JOM
https://doi.org/10.1007/s11837-024-06789-8
© 2024 The Minerals, Metals & Materials Society

ADVANCES IN BIOMATERIALS AND MATERIALS FOR BIOMEDICAL APPLICATIONS

Tannic Acid-Loaded MgO and ZnO-Doped Antibacterial Hydroxyapatite for Orthopedic and Dental Applications

CLAIRE PUTELLI,[1] JOEL PILLI,[1,2] GWENEVERE GATTO,[1,2]
and ARJAK BHATTACHARJEE [1,3]

1.—Sustainable Manufacturing and Tissue Engineering Laboratory, Department of Materials and Metallurgical Engineering, New Mexico Institute of Mining and Technology, Socorro, NM 87801, USA. 2.—Department of Biology, New Mexico Institute of Mining and Technology, Socorro, NM 87801, USA. 3.—e-mail: arjak.bhattacharjee@nmt.edu

Hydroxyapatite (HA)-based materials are utilized as a bioactive ceramic for musculoskeletal reconstruction, owing to their chemical similarities to bone. However, they do not have any inherent antibacterial properties. Hence, post-surgical bacterial infection on HA scaffolds may cause osteomyelitis that needs to be rectified with costlier and more painful revision surgery. Our research aims to dope HA with transition metal oxides, such as ZnO and MgO, followed by loading tannic acid (TA) as an alternate antibacterial agent for various orthopedic and dental applications. The phase and microstructural investigation studies show no adverse effect as a result of doping. The combined effects of dopants and TA lead to $\sim 98\%$ antibacterial efficacy against *S. aureus* after 24 h of sample–bacterial interactions. The selected compositions do not show any adverse effects on the NIH3T3 cell line. In summary, our work proposes an alternate strategy to fabricate an antibacterial scaffold with TA-loaded ZnO and MgO-doped HA for various orthopedic and dental applications.

INTRODUCTION

There has been a global increase in cases of musculoskeletal disorders, birth defects, war injuries, bone cancer, and other bone-afflicting conditions has which motivated scientists to discover new, more effective treatments for bone reconstruction.[1,2] Various musculoskeletal disorders result in a total US$136.8 billion yearly burden to the United States economy.[3] The current treatment approach to skeletal reconstruction is by autologous bone grafts; however, that needs multiple site surgeries and may lead to complications.[4] In this regard, artificial scaffolds with bone-like material are useful. Hydroxyapatite [HA, $Ca_{10}(PO_4)_6(OH)_2$] has been thoroughly evaluated by bone researchers because of its biocompatibility and chemical similarities to bone.[5,6] Few recent pioneering works have investigated the potential of HA with natural polymers for patient-specific tissue engineering applications.[7–9] HA has recently been utilized in different types of additive manufacturing to prepare complex scaffolds for bone regeneration.[10,11] Although synthetic HA displays appropriate outcomes in bone tissue engineering, it does not have any inherent antibacterial properties and shows limited osteogenic potential without any further chemical modifications or growth factor addition.[12–15] Bacterial infection on the HA scaffold surface may lead to post-surgical infection and implant failure, which can lead to costlier, painful revision surgery and further complications. Additionally, using antibiotics does not guarantee adequate protection against bacterial strains because of two reasons: (1) site-specific antibiotic delivery is challenging, and (2) bacterial resistance to several antibiotics.[16–18] An alternate approach is to dope HA with various cations, primarily transition metals, to improve the antibacterial activity at the implanted site, as they are not cytotoxic at low concentrations.[18,19] The flexible crystal chemistry of HA allows

---

Claire Putelli and Joel Pilli have contributed equally to this work.

(Received April 10, 2024; accepted July 22, 2024)

Published online: 04 September 2024

the doping of metal ions and non-metal ions in the cationic and anionic sites, respectively.[15,20,21] The addition of dopants into HA not only enhances its biological activity but also assists in enhancements in crystallinity and mechanical properties.[22–24]

The major scientific question posed in this work is: can we utilize MgO- and ZnO-doped HA with plant-sourced tannic acid (TA) to fabricate an alternate antibacterial and cytocompatible scaffold for various bone tissue engineering applications? In this work, we specifically selected zinc oxide (ZnO) and magnesium oxide (MgO) as dopants with HA due to their inherent antibacterial potential and positive effects on new bone formation. The novelty of this work lies in the direct incorporation of plant-sourced TA on the doped HA scaffolds followed by the evaluation of biological properties. Zinc (Zn) is one of the essential trace elements that contribute to many enzymes regarding bone metabolism.[25] Previous works have reported that HA doped with Zn ions (Zn^{2+}) increases the proliferation and differentiation of osteoblast cells, and helps in bone growth and healing due to injury.[26] Additionally, Zn^{2+} addition to HA leads to antimicrobial properties against Gram-positive and -negative bacteria that are found at the implantation location such as *Staphylococcus aureus* (*S. aureus*), *Escherichia coli* (*E. coli*), etc.[27–30]

Due to these biological properties of Zn^{2+}, we selected it as one of the dopants in this work. The other important transition metal for new bone formation is Mg^{2+}, which acts analogously as a growth factor during the early phases of osteogenesis and encourages bone development.[31–33] Additionally, both Mg^{2+} and Zn^{2+} are essential nutrients and are connected to biological apatite. Mg^{2+} plays an important role in the defined movement of the musculoskeletal systems. Furthermore, it accelerates bone formation and revitalizes mesenchymal stem cells to prompt osteogenic differentiation.[34] Previous works demonstrated that Zn^{2+}- and Mg^{2+}-doped HA leads to differentiation of the mesenchymal stem cells to bone-forming osteoblast.[35–37] This study aims to use MgO and ZnO co-doped HA as an alternate antibacterial scaffold by directly incorporating the drug. In this regard, we have selected a natural medicinal compound, TA, instead of commercially available synthetic drugs. The utilization of natural medicinal compounds to treat various diseases is gaining momentum in clinical research due to their abundance and fewer side effects compared to many available synthetic drugs. A recent report indicated that one in every five US adults prefers to use natural medicinal compounds.[38] TA is a form of natural polyphenol compound found in fruits and teas.[39] Because of the pyrogallol group, TA has executed good antibacterial and anti-oxidant characteristics, which contribute to its versatile biomedical applications.[40,41] TA forms complexes with various metals and also adheres to the surface of several substrates.[42–45] Hence, it has been widely utilized in dental implants. Previous works have also reported that TA is widely utilized as a green cross-linker and helpful in improving the corrosion resistance of HA.[42,45]

There is a knowledge gap in the existing literature investigating the effects of direct incorporation of TA in doped HA for various bone-related applications. Our work aims to bridge that gap. The objective of this study is to design a novel scaffold with ZnO and MgO co-doped HA followed by the direct incorporation of TA for bone tissue engineering. The hypothesis is that the combined effects of TA, ZnO, and MgO will incorporate antibacterial efficacy without compromising cytocompatibility. Our results indicate successful fabrication of ZnO and MgO Co-doped HA followed by TA loading. The designed multifunctional scaffold shows enhanced antibacterial efficacy without compromising cytocompatibility.

EXPERIMENTAL

Sample Fabrication

The ZnO and MgO doping in commercial HA powder (NEI, USA) were carried out using 0.25 wt.% and 1 wt.%, respectively, by 2 h of ball milling at a speed of 80 with a 1:2 powder-to-ball ratio. The ZnO (Cas # 1314-13-2; 99.9%) and MgO powder (Cas # 1309-48-4 ≥ 96.0%) used in this study were purchased from Alfa Aesar. The doping amount was selected according to previously reported optimization studies and corresponding mechanical and biological results.[1,21,46] The powders were pressed uniaxially for 2 min using a hydraulic press. As previously mentioned, the pressed powders were sintered at 1250°C, with a 2-h holding.[47] Here, the undoped HA will be denoted as HA, the ZnO-doped HA samples will be referred to as ZHA, the MgO-doped HA samples will be denoted as MHA, and the ZnO and MgO co-doped samples will be referred to as MZHA.

Measurement of Densification and Dimensional Shrinkage

The bulk density and theoretical density of the samples were measured to quantify the densification after sintering. The volume shrinkage was calculated by measuring the dimension change for volume after sintering concerning the volume of the green compacts. The radial and longitudinal shrinkage were similarly measured with the change of diameter and height after sintering ($n = 3$).[47]

Phase and Microstructural Investigation

The x-ray diffraction (XRD; Empyrean; PANalytical) measurement of the samples was performed in the range, $20° \leq 2\theta \leq 60°$, with a step size: 0.015° (400 s/step). Cu-K1α radiation of 1.54 Å was utilized at a voltage and current of 45 kV and 40 mA, respectively. Characterization of the functional groups of HA, MHA, ZHA, and MZHA was performed by Fourier-transform infrared spectroscopy (FTIR; Nicolet Is50 FTIR; Thermo Scientific), in the range of 500–2000 cm^{-1}. The resultant microstructures after ZnO and MgO doping were analyzed using field-emission scanning electron microscopy (FESEM); the images were collected at a voltage of 15 kV with a magnification of × 5000. A layer of platinum was applied before performing FESEM to make the samples conductive. To understand the morphological changes in the powder as a result of doping, FESEM of HA and ZnO- and MgO-doped HA was performed. Additionally, energy dispersive spectroscopy (EDS) was carried out to find the elemental composition in the undoped and doped samples.

Tannic Acid Loading and Characterization

An ethanolic solution of TA (98.0%, Millipore Sigma, St. Louis, USA) was made at a concentration of 7 mg/mL. This was loaded on top of each scaffold by pipetting a low amount (30 μg) and a high amount (560 μg) followed by an assessment of cytocompatibility and antibacterial activity. The samples with 30 μg TA are represented by the suffix T1, whereas the samples with 560 μg TA are denoted with a suffix T2, with each compositional notation mentioned before each sample.

Functional groups of TA were identified with FTIR spectra in the range 500–4000 cm^{-1}. A diluted ethanolic solution of TA was tested in the 200–400 nm range using ultraviolet-visible (UV-VIS; Evo260; Thermo Scientific) to find the characteristic absorbance peak.

Antibacterial Efficacy Testing

Modified ISO 22196: 2011 Standard for Agar Plate Colony Count

The measure of the antibacterial activity against *S. aureus* was conducted according to the modified ISO 22196: 2011 Standards, as reported in previous works.[16] The freeze-dried bacterial stock was purchased from Carolina Biological Supply (Burlington, NC, USA). After bacterial activation, measurements of the optical densities of bacterial suspensions at different concentrations were conducted with a UV–Vis spectroscopy microplate reader (Accuris smartreader 96-T) and compared to the McFarland standard.[16,31] The sterilized samples were put in 24-well plates with 10^5 CFU of bacteria placed on top, and then 1 mL broth media was added. The well plates were incubated at 37°C for 24 h. In the next step, the samples were moved to glass vials, mixed with 1 mL phosphate buffer solution (PBS), vortexed for 15 s followed by serial dilution, and then 10 μL of the vortexed & diluted solution was plated on agar plates via streaking. The streaked plates were then incubated at 37°C for 24 h, followed by photography to count the bacterial colonies. The antibacterial efficacy was quantified as 100 – bacterial cell viability (%), where the following equation defines bacterial cell viability (%):

$$\text{Bacterial cell viability }(\%) = X_{\text{treatemnt}}/X_{\text{control}} \times 100\%$$

Morphological Characterization

Using FESEM, the bacterial morphology was analyzed and determined. Sample fixation was performed with 2% paraformaldehyde and 2% glutaraldehyde in 0.1 M PBS and then refrigerated overnight at a temperature of 4°C. In the next step, rinsing of each sample was performed with 0.1 M PBS, and ethanolic dehydration was carried out in concentrations of 30%, 50%, 70%, 95%, and 100% three times.[16,31] The dehydrated samples were placed inside a fume hood overnight for Hexamethyltiisilizane (HMDS) drying, and then the surface was coated with platinum using a sputter coater.

Assessment of Cytocompatibility

Cell Seeding on Sample Surfaces

To assess the effects of doping and TA loading on cytocompatibility, a cell–material interaction study was carried out with an NIH3T3 fibroblast cell line (ATCC, USA). The cell culture experiment used Dulbecco's modified Eagle's medium, supplemented with 10% fetal bovine serum, and 1% penicillin/streptomycin.[15] The sterilized samples after autoclave and drug loading were kept in 24-well plates and, on each sample top, a cellular density of 20,000–25,000 was seeded followed by the addition of 1 mL culture media. Each well plate was incubated at 37°C for 24 h within a 5% CO_2 atmosphere.

MTT Assay and Cell Viability Quantification

The cell viability was quantified using MTT (3-(4,5-dimethylthiazol-2-yl)-2,5-diphenyl tetrazolium bromide) assay after cell–material interaction for 1 day and 3 days. First, the samples were moved to a fresh well plate followed by the addition of 100 μL MTT solution and 900 μL of media. The MTT and media-added samples were incubated for 2 h at 37°C. Post-incubation, the media was replaced with 600 μL of MTT solubilizer, and the resultant optical density (100 μL solution) was measured using the UV–VIS microplate reader. The cell viability was assessed from the obtained results. The biological experiments were carried out in triplicate.[48,49]

RESULTS

Doping HA with MgO and ZnO powder using ball milling followed by hydraulic pressing, sintering, and obtained representative samples are schematically shown in Fig. 1. Table I displays the bulk density (g/cm^3) and densification shrinkage, volume, radial, and longitudinal shrinkage (%) after sintering. The bulk densities were: HA 2.7 ± 0.1 g/cm^3, ZHA 2.6 ± 0.2 g/cm^3, MHA 2.5 ± 0.1 g/cm^3, and MZHA 2.8 ± 0.3 g/cm^3, while the densification shrinkage were HA 86.3 ± 1.7%, ZHA 82.8 ± 2.1%, MHA 86.3 ± 3.8 %, and MZHA 88.2 ± 2.4%. HA had a volume, radial, and longitudinal shrinkage of 57.2 ± 2.5%, 24.3 ± 0.4%, and 24.2 ± 1.7%, respectively; for ZHA they were: 58.7 ± 3.4%, 25.5 ± 0.3%, and 25.7 ± 4.2%, respectively; for MHA they were: 61.2 ± 0.5%, 39.5 ± 0.8%, and 32.1 ± 6.2%, respectively; and for MZHA they were: 61.5 ± 4.7%, 31.3 ± 1.1%, and 39.1 ± 4.2%, respectively.

The XRD results for the sintered samples in the range 20°–60° are shown in Fig. 2a. The standard peaks of HA are observed and marked in the figure. The HA phase is confirmed from JCPDS #09–0432.[2] Doping HA with MgO and ZnO does not result in any adverse effects on the phase formation after sintering. The FTIR spectrum presented in Fig. 2b shows the vibrational modes of undoped and doped HA in the 500- to 1300-cm^{-1} range. The bending mode of the PO$_4^{3-}$ group is noticed in the ~ 560–610-cm^{-1} range. The corresponding stretching vibrations appear around ~ 970–1100 cm^1. The vibrational mode at ~ 670 cm^{-1} is attributed to the OH groups.[50] Figure 3a, b, c, and d displays the sintered samples under FESEM. There are distinct grain boundaries, indicating that all the powder has been fully sintered.[51,52] Additionally, no significant difference in morphology is noticed across the compositions because of the doping. The EDS results in Fig. 3e and f show the elemental analysis of the HA powder and the MgO-doped HA powder. Peaks of corresponding elements in HA, i.e., Ca, P, and O are observed in the spectra. The MgO-doped powder spectra show Mg peaks along with the peaks of Ca, P, and O, indicating successful doping with the HA. The FESEM images of the HA powder and the ZnO- and MgO-doped HA powder

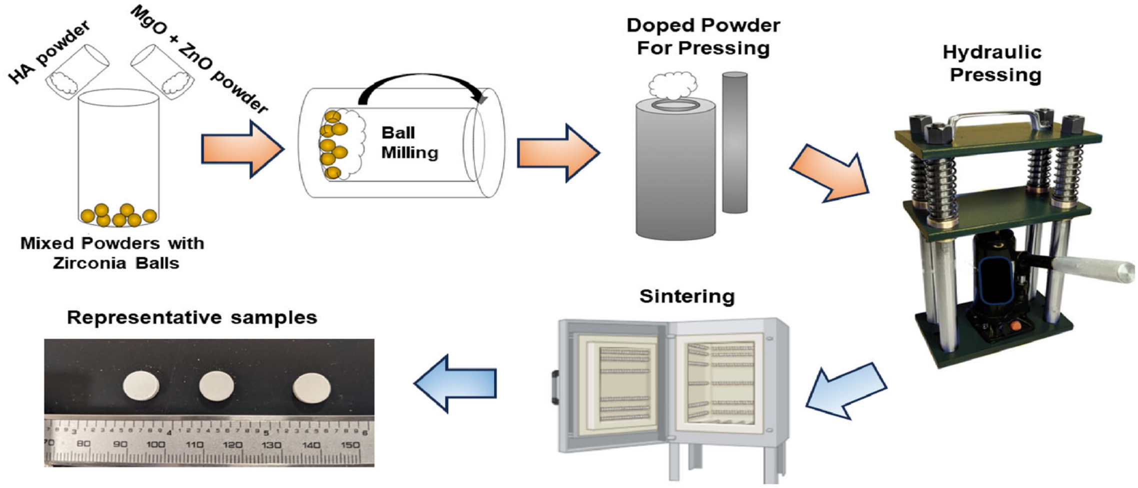

Fig. 1. Schematic of the sample preparation process starting from doping HA with MgO and ZnO, followed by hydraulic pressing and sintering; representative images of fabricated doped/undoped samples are shown.

Table I. The bulk density (g/cm^3), shrinkage as a result of densification, volume, radial, and longitudinal shrinkage (%) after sintering, respectively

Sample ID	Bulk density (g/cm^3)	Densification shrinkage (%)	Volume shrinkage (%)	Radial shrinkage (%)	Longitudinal shrinkage (%)
HA	2.7 ± 0.1	86.3 ± 1.7	57.2 ± 2.5	24.3 ± 0.4	24.2 ± 1.7
ZHA	2.6 ± 0.2	82.8 ± 2.1	58.7 ± 3.4	25.5 ± 0.3	25.7 ± 4.2
MHA	2.5 ± 0.1	86.3 ± 3.8	61.2 ± 0.5	39.5 ± 0.8	32.1 ± 6.2
MZHA	2.8 ± 0.3	88.2 ± 2.4	61.5 ± 4.7	31.3 ± 1.1	39.1 ± 4.2

All samples show a similar range of bulk density and densification (~ 83–88%) after the conventional sintering process. The corresponding volume, radial, and longitudinal shrinkage data support this observation.

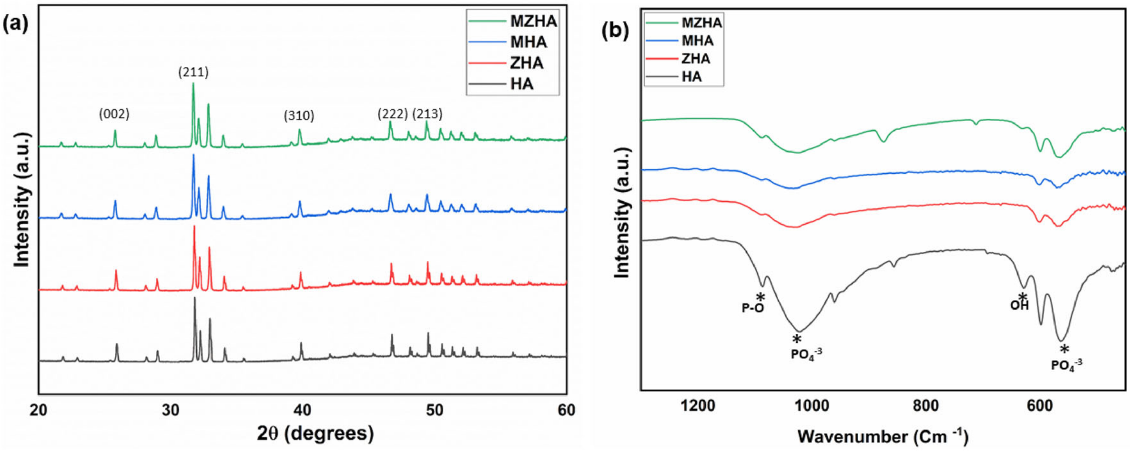

Fig. 2. (a) XRD peaks of HA co-doped with ZnO and MgO (*MZHA*), HA doped with MgO (*MHA*), HA doped with ZnO (*ZHA*), and undoped HA (*HA*), in the range of 20°–60°. The standard peaks of HA are observed and marked in the figure. (b) FTIR spectra of the samples showing standard peaks of PO_4^{3-} and OH in the 1300–500-cm^{-1} range. The XRD and FTIR images indicate the retention of HA after doping.

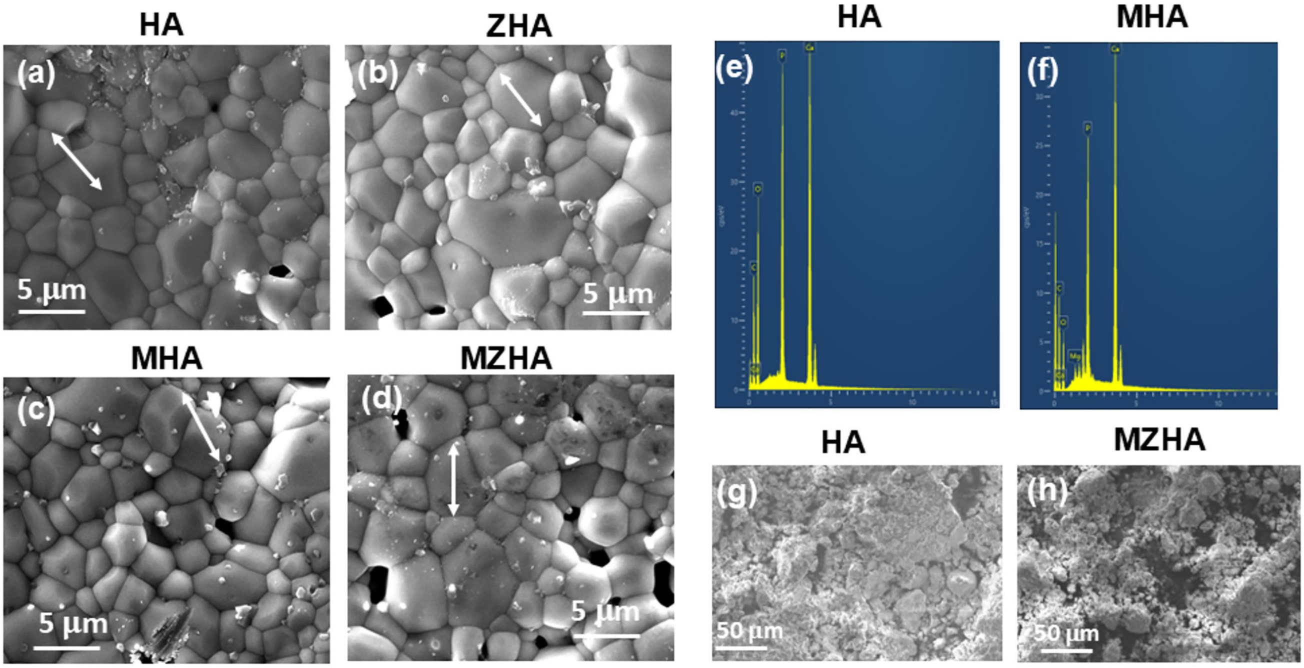

Fig. 3. FESEM images displaying the morphology of the sintered samples: (a) *HA*, (b) *ZHA*, (c) *MHA*, and (d) *MZHA*, respectively. Representative grains in the sintered body are marked with white arrows, (e) the EDS spectra of HA show peaks of Ca, P, and O, (f) the EDS spectra of MHA show peaks of Mg, Ca, P, and O, (g) morphology of HA powder, and (h) morphology of MZHA powder.

are shown in Fig. 3g and h, respectively. Agglomerated powder morphology of varying particle size is seen in the corresponding images. The FTIR spectra of TA are shown in Fig. 4a. The prominent peaks displayed are the OH, C-H, C=O, and C-O bonds. At ~ 3275 cm^{-1}, hydroxyl groups display adsorption; additionally, an OH stretch is noted near 2211–3277 cm^{-1} and an alkane is observed at 2833 cm^{-1}. These spectra agree well with previously reported works.[53] The UV–VIS spectra of TA are shown in Fig. 4b. The major TA peak is shown at ~ 271 nm with a weak peak at ~ 214 nm. This observation is well supported by previously reported works.[54,55] A few other works have reported that, at a lower pH, the peak at ~ 213 nm disappears but returns weakly after a pH of 7.[56]

The cytocompatibility results of the tested samples are shown in Fig. 5, confirming that no compositions are cytotoxic according to the ISO 10993 standard.[50] On day 1, similar cell viability is noticed for the HA and HAT2 samples. However, the MZHAT2 sample shows a significantly enhanced cell viability on day 1. On day 3, both the treatment compositions show enhanced cell viability compared

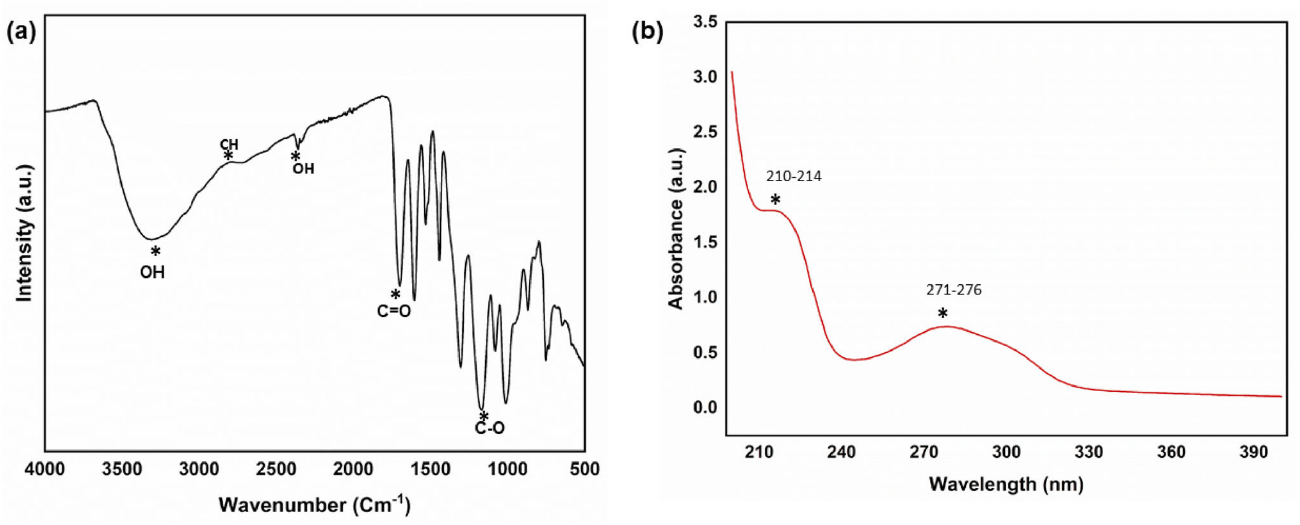

Fig. 4. (a) FTIR spectra of TA in the 4000–500-cm^{-1} range. Standard peaks of TA such as OH, C=O, CH, etc., are observed in the spectra and marked with *, (b) UV–VIS spectra of TA in the 200–400-nm range show the highest absorbance in the ~ 275-nm region. The FTIR and UV–VIS spectra agree well with available literature reports.

with the control. The cell viability increased in the TA-loaded compositions on day 3 compared to that on day 1. Since a higher amount of TA loading (560 μg) does not show any cytotoxicity, it was selected for further antibacterial efficacy assessment against *S. aureus*, and the assessment results are shown in Fig. 6a, b, and c. The agar plate images (Fig. 6a) show denser colonies in the control HA sample, whereas a significant reduction in bacterial colonies is noticed in the treatment MZHAT2 sample. The quantification of the bacterial colonies (Fig. 6b) indicates that the treatment sample shows up to ~ 98% antibacterial efficacy. The FESEM images (Fig. 6c) after bacteria culture show a higher density of bacterial colonies on the control HA sample. The TA-loaded MgO- and ZnO-doped HA sample results in a significant reduction in the colonies. A dotted circle is used in the FESEM images to mark the bacterial colonies.

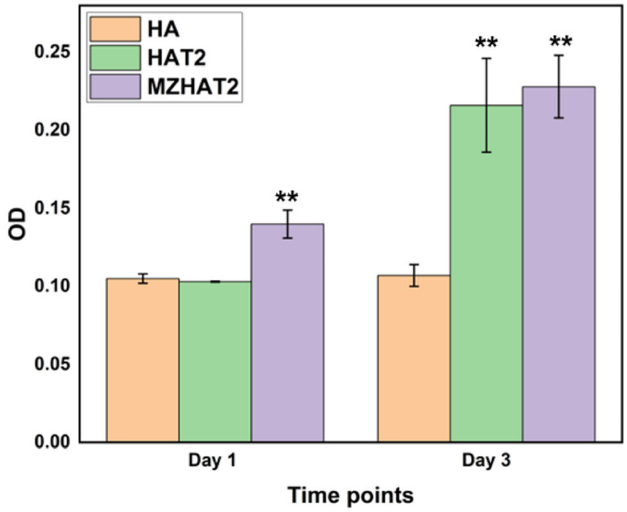

Fig. 5. The MTT assay after 1 day and 3 days interactions of tested samples with NIH3T3 cells indicates that no compositions are cytotoxic. The MZHAT2 composition shows more enhanced cell viability than the control on day 1. On day 3, both the treatment samples show significantly more enhanced cell viability than the control.

DISCUSSION

Clinical Significance of Antibacterial Scaffolds for Orthopedic and Dental Applications

Osteomyelitis is a clinical condition, resulting from the growth of bacteria on the bone implant surface.[16] It is one of the leading causes of implant failure that may need to be corrected by revision surgeries.[21,57] One recently published clinical study on patients with orthopedic infection documents that *S. aureus* is the major microorganism that causes bacterial infection in patients after orthopedic surgery. *S. aureus* alone accounts for ~ 38% of infection in all investigated patients, the highest among all tested microorganisms.[58] Currently, antibiotic treatments are prescribed to patients with osteomyelitis.

However, antibiotic delivery to a specific surgery site throws a significant clinical challenge. Additionally, the emergence of drug-resistant bacteria is another important concern in this regard.[59,60] We propose an alternate strategy for fabricating bone tissue engineering scaffolds with inherent antibacterial properties, and selected dopants such as ZnO and MgO with HA, and a natural medicinal compound, TA. The antibacterial results (Fig. 6a and b) show that the combined effects of dopants and TA

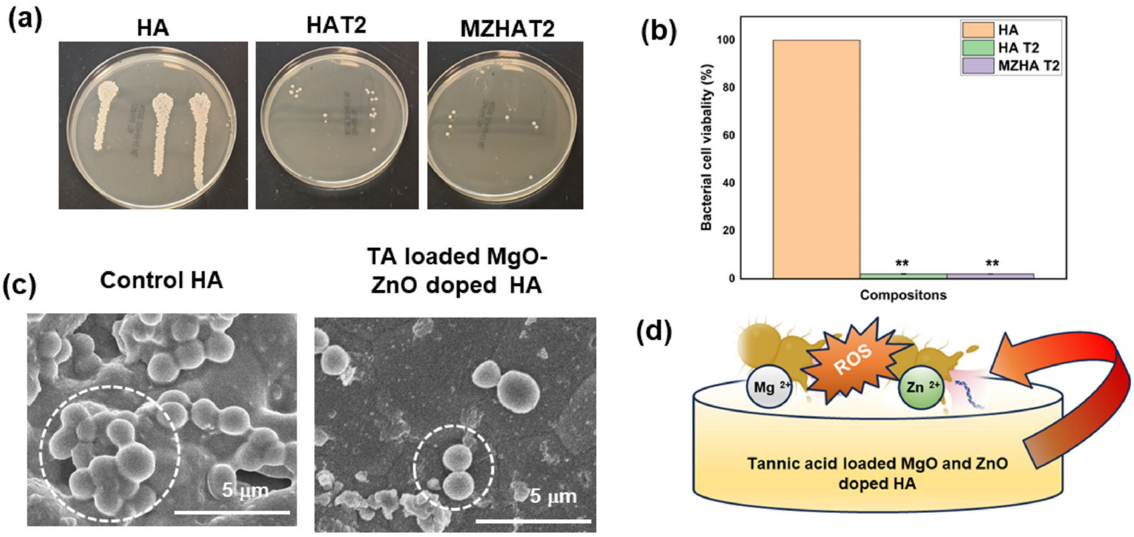

Fig. 6. Antibacterial efficacy according to modified ISO 22196. 2011 standards after 24 h of sample bacteria interaction shows (a) dense bacterial colony formation is noted in the HA sample while the treatment samples, i.e. TA- loaded HA, TA-loaded ZnO- and MgO-doped HA displays a significantly reduced bacterial colony formation on the agar plates, (b) quantification of the bacterial cell viability shows that the treatment compositions show up to ~ 98% antibacterial efficacy after 24 h of sample–bacterial interactions (**$P < 0.0001$), (c) FESEM images show denser bacterial colonies on the control HA sample. The TA-loaded ZnO- and MgO-doped HA sample shows a significant reduction in bacterial colonies. A dotted circle marks the colonies, and (d) schematic of the antibacterial mechanism due to TA, ZnO, and MgO.

lead to up to ~ 98% antibacterial efficacy against osteomyelitis causing *S. aureus* compared to the control. Assessment of antibacterial efficacy after direct incorporation of TA into ZnO- and MgO-doped HA is a novel finding of this study.

Doped Hydroxyapatite as a Scaffolding Material for Bone Tissue Engineering

The demand for skeletal reconstruction among younger patients is increasing worldwide, owing to modern and active lifestyles. One statistical prediction indicates an increase in total hip arthroplasty up to ~ 71% by the year 2030, among which a significant number of surgeries are expected in younger patients, who are less than 65 years.[21,61] These statistics indicate the need to fabricate artificial bone-like scaffolds with a longer service life. Additionally, the inherent antibacterial properties of the scaffolds will be helpful in minimizing the chances of revision surgery. In this regard, our approach is to dope HA with antibacterial and osteogenic transition metals, like ZnO and MgO. Previous works have reported that both these dopants are beneficial for bone growth after scaffold implantation.[31,50] The phase analysis results, such as XRD (Fig. 2a) and FTIR (Fig. 2b) of HA and doped HA indicate that doping with these transition metals does not cause any adverse effects in terms of HA phase formation, and similar phases are seen in both the doped HA and undoped HA samples. A similar observation was reported in previous works.[15,62] When doping HA with cationic dopants such as ZnO, and MgO, the cations Zn^{2+} and Mg^{2+} replace the corresponding sites of Ca^{2+} in the HA structure. Ca^{2+} has a radius of 1.00 Å, whereas the radius of Zn^{2+} is 0.74 Å and that of Mg^{2+} is 0.65 Å.[63] Prior works have suggested that substituting HA with smaller cations leads to a reduction in the unit cell volume of the doped HA compared to undoped HA.[50,63] However, when the doping amount is lower, it does not cause any significant secondary phase formation. Our doping amount was small, hence no adverse phase formation was noticed in XRD. A lower amount of doping also does not lead to any significant changes in the functional groups of HA and doped HA. This observation of both XRD and FTIR is well supported by previously works.[50,63,64]

The microstructural analysis by FESEM (Fig. 3a, b, c, and d) indicates a similar morphology of the doped and undoped samples. The effect of sintering is evidenced by distinct grain boundaries in the microstructure. The densification results (Table I) agree well with the microstructural observation. A sintered density of up to ~ 88% is observed in the tested samples. Previous works on the densification of HA or doped HA by conventional sintering indicate a similar range of sintered density for the tested samples.[65] The elemental composition of HA is confirmed from the EDS spectra (Fig. 3e). In the doped sample's EDS spectra, peaks of Mg are visible (Fig. 3f), which indicate successful doping in HA. Previous works analyzed the influence of MgO and ZnO doping on the mechanical properties of HA and tricalcium phosphates. It has been reported that both dopants significantly increase the compressive strength of HA.[66] MgO is comparatively better in terms of compressive strength enhancement than ZnO. Other works have also reported a similar observation of compressive strength increase in MgO-doped 3D-printed tricalcium phosphate after sintering.[67] MgO is a well-known sintering additive that promotes densification and grain boundary-strengthening effects.[68] This leads to the enhancement in the compressive strength of the MgO-doped HA.

Tannic Acid as an Alternate Antibacterial and Cytocompatible Agent

The effectiveness of various natural medicinal compounds to treat clinical disorders is well documented in ancient Indian medicinal literature, *Ayurveda*.[16] Modern scientific research has proven the underlying mechanism by which many of these natural medicinal compounds show different therapeutic potentials. The use of these natural medicinal compounds directly onto bone tissue engineering scaffolds is gaining momentum in scientific research.[16,31] Our strategy has been to use TA, an extract of tea plants and fruits, after direct incorporation into HA-based scaffolds. The functional group analysis of TA by FTIR (Fig. 4a) and UV–VIS spectra (Fig. 4b) agree well with previous works.[53,54] TA has several therapeutic potentials, such as antimutagenic, antitumor, and anti-oxidating characteristics. Additionally, it is a known homeostatic agent. It has also been determined that TA has chemo-preventive potential.[69] Presently, TA is being evaluated as an organic polymer additive because it displays bioactive characteristics and improves the properties of materials for biomedical uses. It is an active compound when used in nutritional products and different types of consumables.[70–72] Our approach has been to investigate the antibacterial properties of TA-loaded ZnO- and MgO-doped HA against osteomyelitis-causing *S. aureus*. The results (Fig. 6a and b) show that a combination of dopants and TA shows up to ~ 98% antibacterial efficacy. The effectiveness of TA against bacteria is expounded by TA's capability to pass through the bacterial cell wall up to the internal membrane, hindering the metabolism of the cell and, because of this, the annihilation of the cell.[73] Furthermore, the sugar and amino acid acceptance are inhibited by TA which restricts the bacteria growth.[74] On the other hand, the utilized dopants, such as ZnO and MgO, also have antibacterial properties. ZnO is a transition metal oxide with a highly oxidative nature, and generates reactive oxygen species (ROS) as the conduit of bactericidal action that kills bacteria and also reduces bacterial adhesion on the Zn^{2+}-containing surfaces.[16] Zn^{2+} damages bacterial cell membrane permeability and influences the metabolism of amino acids. Additionally, it reacts with some of the primary energy groups of proteins, nucleic acids, and biological enzymes to delay the growth of bacteria. Zn^{2+} ions stop some metabolic conduits in bacteria that lead to their death.[75,76] Specifically, Zn^{2+} binds with PsaBCA transporters inside the bacteria and hinders the uptake of Mn^{2+} by the bacteria. Mn^{2+} is an essential element for bacterial nutrition and also helps in the protection of bacterial cells against oxidative stress.[77] One publication about the antibacterial properties of Mg^{2+} reports that Mg^{2+}-containing bone implants show antibacterial efficacy against methicillin-resistant *S. aureus*, a standard osteomyelitis-producing bacterium.[78] One of the major mechanisms by which Mg^{2+} shows similar antibacterial efficacy is the generation of ROS to that of Zn^{2+}. A few previous works have documented that, after the interaction of bacteria with Mg^{2+}-containing surfaces, a proton electrochemical gradient is created that causes bacterial death by interrupting the synthesis of adenosine triphosphate.[79] The FESEM results (Fig. 6c) in our study indicate that the presence of TA and ZnO and MgO dopants leads to a significant reduction in bacterial colonies compared to the control. The proposed antibacterial mechanism is shown in Fig. 6d.

The cytocompatibility assessment after day 1 and day 3 indicates that no composition is cytotoxic as per the ISO 10993 recommended standard.[21] The combined effects of the dopants and TA lead to a significant increase in cellular viability than the control (Fig. 5). Hence, TA-loaded ZnO and MgO-doped HA could be a promising material for various tissue engineering applications.

Contributions to Science and Direction to Future Research

The scientific contributions of our work can be summarized as (1) the utilization of TA-loaded ZnO- and MgO-doped HA as an alternate multifunctional scaffold for bone tissue engineering, and (2) the investigation of antibacterial efficacy of the designed scaffolds against osteomyelitis-causing *S. aureus* bacteria. Future works can be directed towards long-term biological studies with this designed alternate system along with the investigation of in vivo bone formation potential.

CONCLUSION

Our work indicates successful fabrication of HA and ZnO- and MgO-doped HA scaffolds using in-house uniaxial pressing followed by the assessment of microstructure and biological properties. The obtained phase analysis by XRD, FTIR, and microstructural analysis by FESEM confirms that co-doping HA with ZnO and MgO does not result in any adverse effects on the phase formation and microstructure. Successful densification of the fabricated samples has been confirmed by density and shrinkage measurements. TA has been used as a novel alternate antibacterial agent after direct incorporation on the scaffold surface. The antibacterial efficacy measurement against *S. aureus* shows ~ 98% antibacterial efficacy due to the combined effects of the dopants and TA. In summary, our work indicates that ZnO and MgO co-doped HA with TA can be used as an alternate scaffold for different types of orthopedic and dental applications.

ACKNOWLEDGEMENTS

The authors would like to acknowledge financial support from the New Mexico Institute of Mining and Technology (NMT) start-up research grant (No. # 103394) to conduct this study. Kind support from the New Mexico INBRE and its NMT liaison Prof. Snezna Rogelj is highly appreciated for the equipment purchase grant to set up AB's new laboratory. The authors would like to thank Mr. Arnob Saha, Ms. Arezou Karimian, Mr. Mason Woodward, Prof. Paul Fuierer, and Prof. Sanchari Chowdhury for helping the authors with various equipment. Kind help from Mr. Anthony Baker and Prof. Michaelann Tartis to conduct the cell culture studies is highly acknowledged by the authors. The subscription version of Biorender.com was used to construct parts of the schematic in Figs. 1 and 6d.

CONFLICT OF INTEREST

The authors declare that there is no conflict of interest or known financial interests/personal relationships that could have appeared to influence the current work of this paper.

REFERENCES

1. D. Ke, A.A. Vu, A. Bandyopadhyay, and S. Bose, *Acta Biomater.* 84, 414 (2019).
2. A. Bhattacharjee and S. Bose, *Mater. Des.* 221, 110903 (2022).
3. A. Litwic, M.H. Edwards, E.M. Dennison, and C. Cooper, *Br. Med. Bull.* 105, 185 (2013).
4. C. Garot, G. Bettega, and C. Picart, *Adv. Funct. Mater.* 31, 2006967 (2021).
5. D.-E. Radulescu, O. R. Vasile, E. Andronescu, and A. Ficai, *Int. J. Mol. Sci.* 24(17) https://doi.org/10.3390/ijms241713157 (2023).
6. W. Chen, L. Nichols, F. Brinkley, K. Bohna, W. Tian, M.W. Priddy, and L.B. Priddy, *Mater. Sci. Eng. C* 120, 111686 (2021).
7. S.L. McNamara, E.M. McCarthy, D.F. Schmidt, S.P. Johnston, and D.L. Kaplan, *Biomaterials* 269, 120643 (2021).
8. M. Farokhi, F. Mottaghitalab, S. Samani, M.A. Shokrgozar, S.C. Kundu, R.L. Reis, Y. Fatahi, and D.L. Kaplan, *Biotechnol. Adv.* 36, 68 (2018).
9. V. Fitzpatrick, Z. Martín-Moldes, A. Deck, R. Torres-Sanchez, A. Valat, D. Cairns, C. Li, and D.L. Kaplan, *Biomaterials* 276, 120995 (2021).
10. J.A. Ayariga, M. Dean, E. Nyairo, V. Thomas, and D. Dean, *JOM* 73, 3787 (2021).
11. A.F. Uehlin, J.B. Vines, D.S. Feldman, D.R. Dean, and V. Thomas, *JOM* 74, 3336 (2022).
12. A. Bhattacharjee, Y. Fang, T. J. Hooper, N. L. Kelly, D. Gupta, K. Balani, I. Manna, T. Baikie, P. T. Bishop, T. J. White, and J. V. Hanna, *Materials (Basel)* 12(11) https://doi.org/10.3390/ma12111814 (2019).
13. Z. Ding, Z. Fan, X. Huang, Q. Lu, W. Xu, D.L. Kaplan, and A.C.S. Appl, *Mater. Interfaces* 8, 24463 (2016).
14. Z.Z. Ding, Z.H. Fan, X.W. Huang, S.M. Bai, D.W. Song, Q. Lu, and D.L. Kaplan, *J. Mater. Chem. B* 4, 3555 (2016).
15. A. Bhattacharjee, A. Gupta, M. Verma, M. P. Anand, P. Sengupta, M. Saravanan, I. Manna, and K. Balani, *Ceram. Int.* 46(1) https://doi.org/10.1016/j.ceramint.2019.08.291 (2020).
16. A. Bhattacharjee and S. Bose, *Biomater. Adv.* 213487 https://doi.org/10.1016/j.bioadv.2023.213487 (2023).
17. F. Zhang, J. Zhuang, Z. Li, H. Gong, B.E.-F. de Ávila, Y. Duan, Q. Zhang, J. Zhou, L. Yin, E. Karshalev, W. Gao, V. Nizet, R.H. Fang, L. Zhang, and J. Wang, *Nat. Mater.* 21, 1324 (2022).
18. P. Sikder and S. B. Bhaduri, in edited by B. Li, T. F. Moriarty, T. Webster, and M. Xing https://doi.org/10.1007/978-3-030-34475-7_24 (Springer International Publishing, Cham, 2020).
19. X. Bai, K. More, C.M. Rouleau, and A. Rabiei, *Acta Biomater.* 6, 2264 (2010).
20. T. White, C. Ferraris, J. Kim, and S. Madhavi, *Rev. Miner. Geochem.* 57, 307 (2005).
21. A. Bhattacharjee, A. Gupta, M. Verma, P. A. Murugan, P. Sengupta, S. Matheshwaran, I. Manna, and K. Balani, *Ceram. Int.* 45(9) https://doi.org/10.1016/j.ceramint.2019.03.132 (2019).
22. D.O. Obada, S.A. Osseni, H. Sina, A.N. Oyedeji, K.A. Salami, E. Okafor, S. Csaki, S.A. Abolade, A. Akande, M. Dauda, L.S. Kuburi, S. Dalhatou, J.K. Abifarin, A.A. Bada, and E.T. Dauda, *J. Aust. Ceram. Soc.* 59, 565 (2023).
23. R. Klinkla, T. Kaewmaraya, A. Bootchanon, T. Saisopa, I. Fongkaew, R. Yimnirun, A. Khamkongkaeo, Y. Rattanachai, and W. Sailuam, *Results Phys.* 57, 107352 (2024).
24. S. Vahabzadeh, M. Roy, A. Bandyopadhyay, and S. Bose, *Acta Biomater.* 17, 47 (2015).
25. D. Lytkina, A. Gutsalova, D. Fedorishin, N. Korotchenko, R. Akhmedzhanov, V. Kozik, and I. Kurzina, J. Funct. Biomater. 11(1) https://doi.org/10.3390/jfb11010010 (2020).
26. S.C. Cox, P. Jamshidi, L.M. Grover, and K.K. Mallick, *Mater. Sci. Eng. C* 35, 106 (2014).
27. R.-J. Chung, M.-F. Hsieh, K.-C. Huang, L.-H. Perng, F.-I. Chou, and T.-S. Chin, *J. Sol Gel Sci. Technol.* 33, 229 (2005).
28. A. Anwar, S. Akbar, A. Sadiqa, and M. Kazmi, *Inorganica Chim. Acta* 453, 16 (2016).
29. N. Ohtsu, Y. Kakuchi, and T. Ohtsuki, *Appl. Surf. Sci.* 445, 596 (2018).
30. S. L. Iconaru, A. M. Prodan, N. Buton, and D. Predoi, *Molecules* 22(4) https://doi.org/10.3390/molecules22040604 (2017).
31. A. Bhattacharjee, Y. Jo, and S. Bose, *J. Mater. Chem. B* 11, 4725 (2023).
32. I. Cacciotti, A. Bianco, M. Lombardi, and L. Montanaro, *J. Eur. Ceram. Soc.* 29, 2969 (2009).
33. P. Sikder, C.R. Grice, and S.B. Bhaduri, *Surf. Coat. Technol.* 374, 276 (2019).
34. C. Wang, K.-J. Jeong, H.J. Park, M. Lee, S.-C. Ryu, D.Y. Hwang, K.H. Nam, I.H. Han, and J. Lee, *J. Colloid Interface Sci.* 569, 1 (2020).
35. D. Bazin, X. Carpentier, O. Traxer, D. Thiaudière, A. Somogyi, S. Reguer, G. Waychunas, P. Jungers, and M. Daudon, *J. Synchrotron Radiat.* 15, 506 (2008).
36. D. Veljovic, T. Matic, T. Stamenic, V. Kojic, S. Dimitrijevic-Brankovic, M.J. Lukic, S. Jevtic, Z. Radovanovic, R. Petrovic, and D. Janackovic, *Ceram. Int.* 45, 22029 (2019).
37. U. Kesarwani, B. Basu, and A.K. Dubey, *Appl. Mater. Today* 36, 102062 (2024).
38. A.N. Welz, A. Emberger-Klein, K. Menrad, and B.M.C. Complement, *Altern. Med.* 18, 92 (2018).
39. L. Qiaoxia, Z. Yujie, Y. Meng, C. Yizhu, W. Yan, H. Yinchun, L. Xiaojie, C. Weiyi, and H. Di, *Colloids Surf. B Biointerfaces* 196, 111304 (2020).
40. D.X. Oh, E. Prajatelistia, S.-W. Ju, H. Jeong Kim, S.-J. Baek, H. Joon Cha, S. Ho Jun, J.-S. Ahn, and D. Soo Hwang, *Sci. Rep.* 5, 10884 (2015).
41. S. Quideau, D. Deffieux, C. Douat-Casassus, and L. Pouységu, *Angew. Chemie Int. Ed.* 50, 586 (2011).

42. L.-Y. Cui, H.-P. Liu, K. Xue, W.-L. Zhang, R.-C. Zeng, S.-Q. Li, D. Xu, E.-H. Han, and S.-K. Guan, *J. Electrochem. Soc.* 165, C821 (2018).
43. H.Y. Son, H. Jun, K.R. Kim, C.A. Hong, and Y.S. Nam, *J. Ind. Eng. Chem.* 63, 420 (2018).
44. C. Zhang, S. Wei, Y. Hu, H. Tang, J. Gao, Z. Yin, and Q. Guan, *J. Colloid Interface Sci.* 512, 55 (2018).
45. B. Kaczmarek, A. Sionkowska, and A.M. Osyczka, *Polym. Test.* 62, 171 (2017).
46. S. Gomes, J.-M. Nedelec, and G. Renaudin, *Acta Biomater.* 8, 1180 (2012).
47. S. Tarafder, V.K. Balla, N.M. Davies, A. Bandyopadhyay, and S. Bose, *J. Tissue Eng. Regen. Med.* 7, 631 (2013).
48. J.C. Boga, S.P. Miguel, D. de Melo-Diogo, A.G. Mendonça, R.O. Louro, and I.J. Correia, *Colloids Surf. B Biointerfaces* 165, 207 (2018).
49. N.J. Fiore, J.D. Tamer-Mahoney, A. Beheshti, T.J.F. Nieland, and D.L. Kaplan, *Biomaterials* 290, 121858 (2022).
50. A. Bhattacharjee, R. Hassan, A. Gupta, M. Verma, P. A. Murugan, P. Sengupta, M. Saravanan, I. Manna, and K. Balani, *J. Am. Ceram. Soc.* 103(8) https://doi.org/10.1111/jace.17077 (2020).
51. T.P. Hoepfner and E.D. Case, *Ceram. Int.* 29, 699 (2003).
52. I.R. Gibson, S.M. Best, and W. Bonfield, *J. Am. Ceram. Soc.* 85, 2771 (2002).
53. T. Wahyono, D. A. Astuti, I. K. Gede Wiryawan, I. Sugoro, and A. Jayanegara, in *IOP Conference Series: Materials Science and Engineering* (IOP Publishing, 2019), p. 42045.
54. Z. Fu and R. Chen, *J. Anal. Methods Chem.* (1) https://doi.org/10.1155/2019/3894571 (2019).
55. A. Barbasz, M. Oćwieja, and J. Barbasz, *Appl. Biochem. Biotechnol.* 176, 817 (2015).
56. T. Shutava, M. Prouty, D. Kommireddy, and Y. Lvov, *Macromolecules* 38, 2850 (2005).
57. E.A. Masters, B.F. Ricciardi, K.L.M. Bentley, T.F. Moriarty, E.M. Schwarz, and G. Muthukrishnan, *Nat. Rev. Microbiol.* 20, 385 (2022).
58. J. Zhang, J. Tu, Y. Chen, and X. Jin, *BMC Microbiol.* 23, 217 (2023).
59. C. Gagliotti, L. D. Högberg, H. Billström, T. Eckmanns, C. G. Giske, O. E. Heuer, V. Jarlier, G. Kahlmeter, D. Lo Fo Wong, J. Monen, S. Murchan, G. S. Simonsen, M. Šubelj, A. T. Andrašević, D. Żabicka, H. Žemličková, and D. L. Monnet, *Euro Surveill. Bull. Eur. Sur Les Mal. Transm. = Eur. Commun. Dis. Bull.* 26(46) https://doi.org/10.2807/1560-7917.ES.2021.26.46.20020941 (2021).
60. G. Mancuso, A. Midiri, E. Gerace, and C. Biondo, *Pathogens* 10, 1310 (2021).
61. A.M. Negm, L.A. Beaupre, C.M. Goplen, C. Weeks, and C.A. Jones, *Arthroplast. Today* 16, 247 (2022).
62. Z. Feng, Y. Liao, and M. Ye, *J. Mater. Sci. Mater. Med.* 16, 417 (2005).
63. D. Ke, S. Tarafder, S. Vahabzadeh, and S. Bose, *Mater. Sci. Eng. C* 96, 10 (2019).
64. D. Predoi, S.L. Iconaru, A. Deniaud, M. Chevallet, I. Michaud-Soret, N. Buton, and A.M. Prodan, *Materials (Basel)* 10, 229 (2017).
65. S. Lala, T.N. Maity, M. Singha, K. Biswas, and S.K. Pradhan, *Ceram. Int.* 43, 2389 (2017).
66. S.J. Kalita and H.A. Bhatt, *Mater. Sci. Eng. C* 27, 837 (2007).
67. G.A. Fielding, A. Bandyopadhyay, and S. Bose, *Dent. Mater.* 28, 113 (2012).
68. F. Sarraf, E. Abbatinali, L. Gorjan, T. Sebastian, P. Colombo, S.V. Churakov, and F. Clemens, *J. Eur. Ceram. Soc.* 41, 6677 (2021).
69. W. Zeng, W. Yu, J. Shen, P. Chen, Z. Shi, G. Xie, Y. Zhang, H. Wang, and N. Guo, *Eur. Polym. J.* 198, 112425 (2023).
70. N. Kumar and N. Goel, *Biotechnol. Rep.* 24, e00370 (2019).
71. T.J. Kim, J.L. Silva, M.K. Kim, and Y.S. Jung, *Food Chem.* 118, 740 (2010).
72. E. Bouki, V.K. Dimitriadis, M. Kaloyianni, and S. Dailianis, *Mar. Environ. Res.* 85, 13 (2013).
73. A. Dabbaghi, K. Kabiri, A. Ramazani, M.J. Zohuriaan-Mehr, and A. Jahandideh, *Polym. Adv. Technol.* 30, 2894 (2019).
74. A. Pandey and P.S. Negi, *Nat. Prod. Res.* 32, 1189 (2018).
75. U. Burman, M. Saini, and P. Kumar, *Toxicol. Environ. Chem.* 95, 605 (2013).
76. N. Iqbal, M.R.A. Kadir, N.H. Mahmood, N. Salim, G.R.A. Froemming, H.R. Balaji, and T. Kamarul, *Ceram. Int.* 40, 4507 (2014).
77. R.M. Couñago, M.P. Ween, S.L. Begg, M. Bajaj, J. Zuegg, M.L. O'mara, M.A. Cooper, A.G. McEwan, J.C. Paton, and B. Kobe, *Nat. Chem. Biol.* 10, 35 (2014).
78. Y. Li, G. Liu, Z. Zhai, L. Liu, H. Li, K. Yang, L. Tan, P. Wan, X. Liu, and Z. Ouyang, *Antimicrob. Agents Chemother.* 58, 7586 (2014).
79. H. Qin, Y. Zhao, M. Cheng, Q. Wang, Q. Wang, J. Wang, Y. Jiang, Z. An, and X. Zhang, *RSC Adv.* 5, 21434 (2015).

Publisher's Note Springer Nature remains neutral with regard to jurisdictional claims in published maps and institutional affiliations.

Springer Nature or its licensor (e.g. a society or other partner) holds exclusive rights to this article under a publishing agreement with the author(s) or other rightsholder(s); author self-archiving of the accepted manuscript version of this article is solely governed by the terms of such publishing agreement and applicable law.